


Article

Photoreduction of CO₂ into CH₄ Using Novel Composite of Triangular Silver Nanoplates on Graphene-BiVO₄

Zhen Zhu ¹, Bo-Xun Jiang ², Ren-Jang Wu ^{2,*}, Cheng-Liang Huang ^{3,*}  and You Chang ⁴

¹ School of Environmental Science and Safety Engineering, Tianjin University of Technology, Tianjin 300384, China; zhenzhu@tjut.edu.cn

² Department of Applied Chemistry, Providence University, Taichung 43301, Taiwan; azsazs74132@gmail.com

³ Department of Applied Chemistry, National Chiayi University, Chiayi City 600355, Taiwan

⁴ Chiou Shang Co., Ltd., Taichung 43301, Taiwan; kg520402@gmail.com

* Correspondence: rjwu@pu.edu.tw (R.-J.W.); clhuang@mail.ncyu.edu.tw (C.-L.H.);

Tel.: +886-4-26328001-15212 (R.-J.W.); +886-5-2717963 (C.-L.H.); Fax: +886-4-26327554 (R.-J.W.)

Abstract: Plasmonic photocatalysis, combining noble metal nanoparticles (NMNPs) with semiconductors, has been widely studied and proven to perform better than pure semiconductors. The plasmonic effects are mainly based on the localized surface plasmon resonance (LSPR) of NMNPs. The LSPR wavelength depends on several parameters, such as size, shape, the surrounding media, and the interdistance of the NMNPs. In this study, graphene-modified plate-like BiVO₄ composites, combined with silver nanoplates (AgNPs), were successfully prepared and used as a photocatalyst for CO₂ photoconversion. Triangular silver nanoplates (TAgNPs), icosahedral silver nanoparticles (I-AgNPs), and decahedra silver nanoparticles (D-AgNPs) were synthesized using photochemical methods and introduced to the nanocomposites to compare the shape-dependent plasmonic effect. Among them, T-AgNPs/graphene/BiVO₄ exhibited the highest photoreduction efficiency of CO₂ to CH₄, at 18.1 μmolg⁻¹h⁻¹, which is 5.03 times higher than that of pure BiVO₄ under the irradiation of a Hg lamp. A possible CO₂ photoreduction mechanism was proposed to explain the synergetic effect of each component in TAgNPs/graphene/BiVO₄. This high efficiency reveals the importance of considering the compositions of photocatalysts for converting CO₂ to solar fuels.

Keywords: CO₂ photoreduction; graphene; CH₄; BiVO₄



Citation: Zhu, Z.; Jiang, B.-X.; Wu, R.-J.; Huang, C.-L.; Chang, Y. Photoreduction of CO₂ into CH₄ Using Novel Composite of Triangular Silver Nanoplates on Graphene-BiVO₄. *Catalysts* **2022**, *12*, 750. <https://doi.org/10.3390/catal12070750>

Academic Editor: Lihua Bi

Received: 13 June 2022

Accepted: 5 July 2022

Published: 7 July 2022

Publisher's Note: MDPI stays neutral with regard to jurisdictional claims in published maps and institutional affiliations.



Copyright: © 2022 by the authors. Licensee MDPI, Basel, Switzerland. This article is an open access article distributed under the terms and conditions of the Creative Commons Attribution (CC BY) license (<https://creativecommons.org/licenses/by/4.0/>).

1. Introduction

Carbon dioxide is a major greenhouse gas that is considered the main reason for global warming [1]. Recently, owing to the rapid depletion of fossil energy, carbon dioxide emissions have significantly increased, leading to serious environmental problems. Thus, many efforts have been made to deal with this problem in recent years [2–6]. To this end, CO₂ photoreduction is one of the most promising green methods to alleviate current environmental issues and energy crises, which converts carbon dioxide into valuable hydrocarbon fuel [5,6].

It is important to design and prepare highly effective photocatalysts to achieve optimal CO₂ photoreduction performance. At this point, a number of photocatalysts have been exploited for CO₂ photoreduction, such as TiO₂ [7,8], NiCO₂O₄ [9], MnS [10], g-C₃N₄ [11], Bi₂WO₆ [12], WO₃ [13], Bi₄Ti₃O₁₂ [14], MoS₂ [15], and so on. Due to its chemical stability, low production cost [16,17], environmental-friendliness, abundance, and appropriate bandgap, bismuth vanadate (BiVO₄) has also been studied as a candidate material for CO₂ photoreduction [16–20]. However, it has some shortcomings, such as the recombination of photoinduced charge carriers and pure BiVO₄ exhibits relatively low CO₂ photoreduction efficiency, which restricts the photocatalytic application of pure BiVO₄ [20]. To solve the above shortcomings, several methods have been developed to improve the CO₂ photoreduction performance of BiVO₄, including surface modification, element doping,

and metal deposition [3,16,18,19]. Table 1 lists conversion rates of CO₂ to CH₄ on several kinds of BiVO₄ photocatalysts, drawing on information from previous studies and from this work [16,18,19]. The constructed series of CdS/BiVO₄ nanocomposites was applied for the CO₂ photoreduction reaction [18]. The optimal photocatalytic reduction rate was measured as 2.1 μmol g⁻¹ h⁻¹ of the activity from converted CO₂ into CH₄ [18]. Flower-shaped g-C₃N₄/Ag/AgCl/BiVO₄ microstructures were fabricated for the conversion of CO₂ to CH₄ [19], which exhibited a CH₄ production rate of 5.3 μmol g⁻¹ h⁻¹. A photocatalyst Cu/BiVO₄ (0.5 wt% Cu) has the photocatalytic activity for CO₂ photoreduction, with a maximum CH₄ production rate of 7.4 μmol g⁻¹ h⁻¹ [16]. Another parameter used to evaluate photoactivity was the quantum efficiency (QE) [15]. The QE of the catalysts was determined as the ratio of the effective electrons used for gas production, such as the CH₄ molecule, to the total input photon flux [15]. The corresponding QE of all photocatalytic activity of samples is summarized in Table 1.

Table 1. Production rate of CH₄ on various BiVO₄ catalysts.

Year/Reference	Photocatalysts /Light Source	Rate of CH ₄ (μmol g ⁻¹ h ⁻¹)	Quantum Efficiency (%)
2018 [18]	CdS/BiVO ₄ 300 W xenon lamp	2.1	–
2018 [19]	g-C ₃ N ₄ /Ag/AgCl/BiVO ₄ 64 W fluorescent lamps	5.3	–
2020 [16]	0.5% Cu/BiVO ₄ 400 W Hg light	7.4	0.19
2021 [17]	0.3% Pd/MgO/BiVO ₄ 400 W Hg light	12.8	0.34
2021 [20]	ZnIn ₂ S ₄ /BiVO ₄	0.3	–
2021 [15]	Ultrathin MoS ₂ film	1.38 nmol/cm ²	0.00007
This work	0.003%AgNPs/ 7% graphene/BiVO ₄ 400 W Hg light	18.1	0.49

– No measurement.

Plasmonic photocatalysis, combining noble metal nanoparticles (NMNPs) with semiconductors, has been widely studied and proven to perform better than pure semiconductors [21–25]. The plasmonic effects are mainly based on the phenomenon called localized surface plasmon resonance (LSPR) of NMNPs. The LSPR is the collective oscillation of conduction electrons on a nanoparticle surface. The LSPR wavelength depends on several parameters, such as size, shape, the surrounding media, and the interdistance of the NMNPs. Triangular silver nanoplates (TAgNPs) are particularly intriguing among all kinds of NMNPs, because the LSPR bands of TAgNPs can be easily adjusted using several physical and chemical methods [26–29]. To compare the plasmonic effects, icosahedral silver nanoparticles (I-AgNPs), decahedra silver nanoparticles (D-AgNPs), and TAgNPs were synthesized using photochemical methods in this study.

In the present investigation, we successfully synthesized TAgNPs/graphene/BiVO₄, and some instrument characterizations were performed. The obtained TAgNPs/graphene/BiVO₄ exhibited about five times higher activity in CO₂ photoreduction than pure BiVO₄. Additionally, we proposed a possible photocatalytic mechanism for CO₂ photoreduction on TAgNPs/graphene/BiVO₄ based on our experimental results.

2. Results and Discussion

2.1. Characterization of Composite Photocatalysts

The chemical composition and crystal structure parameters of materials can be determined using XRD spectra. Figure 1a shows the XRD spectrum of BiVO₄ with characteristic diffraction peaks (2θ) at 18.6°, 28.2°, 30.6°, 34.4°, 35.1°, 39.7°, 42.5°, 46.3°, 46.8°, 50.1°, 53.3°, 58.1°, and 58.4°, which we attributed to the (110), (121), (040), (200), (002), (211), (051), (132), (240), (202), (161), (312), and (016) planes of monoclinic BiVO₄, respectively [30].

Additionally, a small peak at around 21.5° could be indexed to the crystal (002) plane of graphene [31]. Furthermore, the prominent diffraction peak was observed, which is attributable to the (200) plane of Ag [30], as shown in Figure 1b. Using Scherer's equation and XRD data, the mean crystallite sizes of all as-synthesized BiVO_4 samples could be calculated within the range of 24.2–36.5 nm.

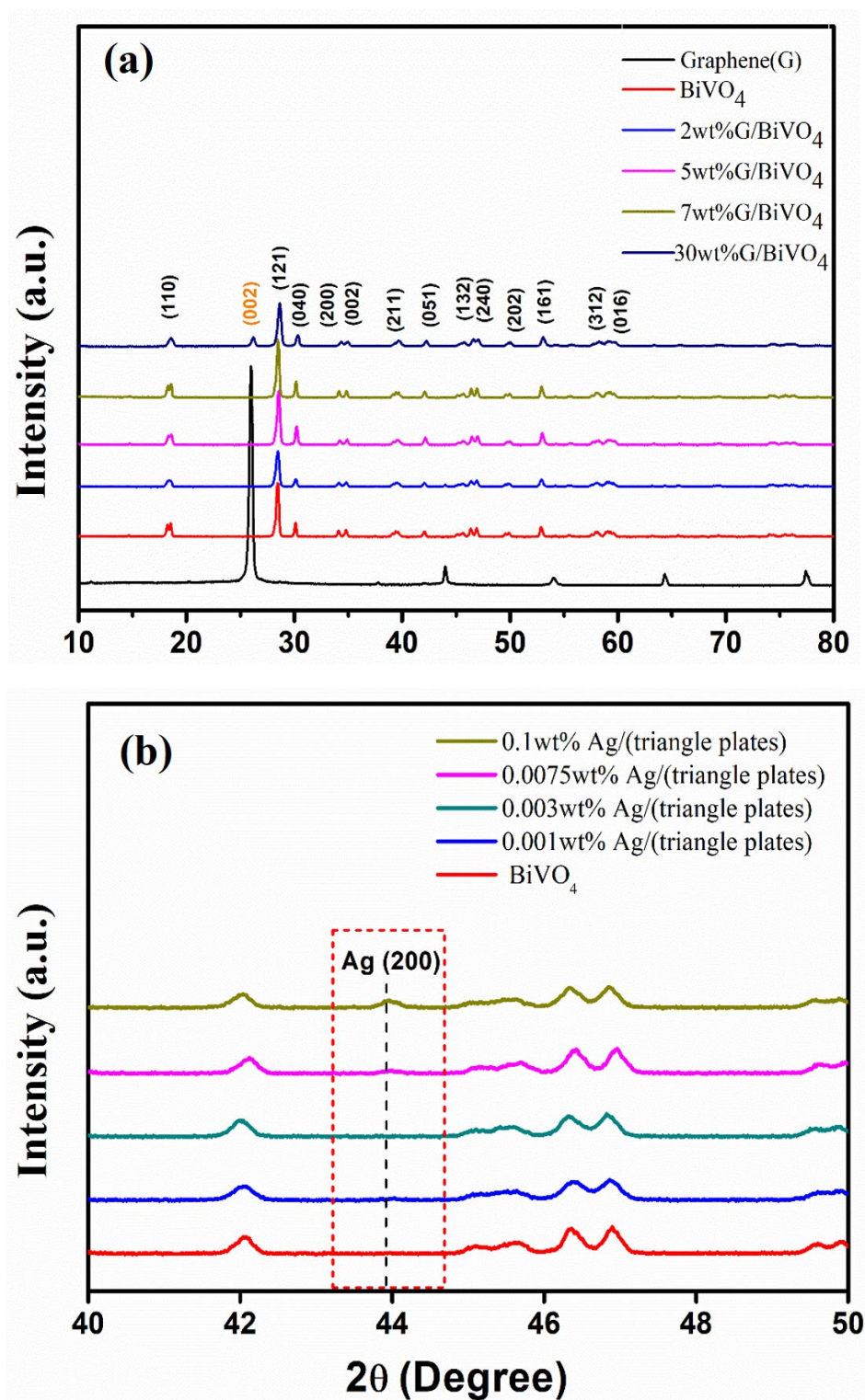


Figure 1. XRD patterns of the obtained photocatalysts (a) in the range of $2\theta = 10^\circ$ – 80° and (b) in the range of 2θ of 40° – 50° .

Figure 2a shows the SEM image of pure BiVO_4 . The plate-like microstructures, with a dimension of 0.4–1.5 μm , indicate that the nano-size BiVO_4 tended to aggregate, possibly due to the shrinkage of the electrical double layer in the sample-preparation drying process for SEM measurement. Figure 2b,c show the SEM images of 7 wt% graphene/ BiVO_4 and TAgNPt/graphene/ BiVO_4 with 0.003 wt% of TAgNPt and 7 wt% of graphene, respectively. These two images also show the plate-like structures, similar to pure BiVO_4 , as shown in Figure 2a. This observation indicates that the addition of graphene and TAgNPt hardly changed the surface properties of composites. In addition, the composites heavily aggregated, such that some AgNPs (marked with red circles) were still observed on the surface of photocatalysts.

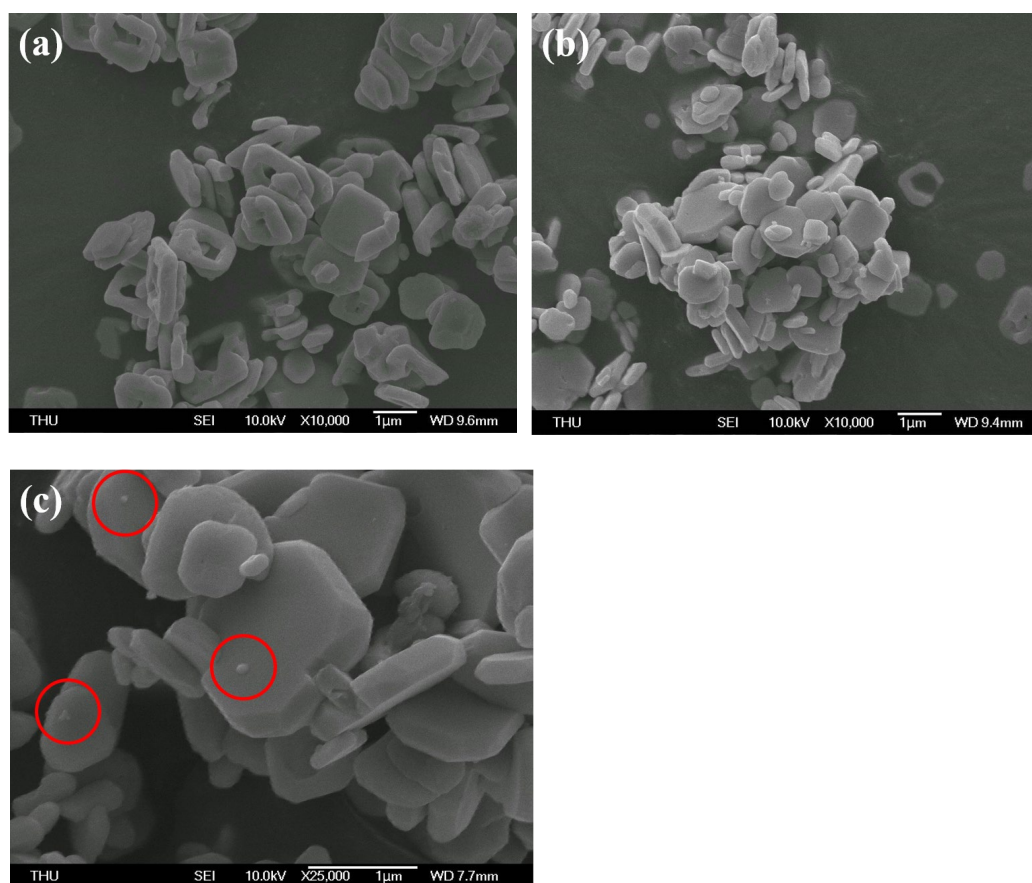


Figure 2. SEM images of the as-prepared (a) BiVO_4 , (b) 7% graphene/ BiVO_4 , and (c) TAgNPt/Graphene/ BiVO_4 with 0.003 wt% of TAgNPt and 7 wt% of graphene.

More detailed structure information of the photocatalysts was obtained using TEM measurements. As illustrated in Figure 3a,b, it can be seen that BiVO_4 and graphene/ BiVO_4 presented lamellar-shaped nanoparticles. The distances between lattice fringes were 0.29 and 0.312 nm, consistent with the d-spacings of (040) and (121) planes of BiVO_4 , respectively [32,33]. Figure 3c depicts the triangular silver nanoplates embedded on the surface of graphene/ BiVO_4 . In addition, the lattice spacing of about 0.204 nm corresponds to the d-spacing of the Ag (200) plane, as displayed in Figure 3d. Energy-dispersive X-ray spectroscopy (EDS) was carried out to further understand the chemical composition of as-synthesized TAgNPt/graphene/ BiVO_4 . As shown in Figure 4, the EDS spectrum revealed the existence of V, Bi, C, Ag, and O in TAgNPt/graphene/ BiVO_4 .

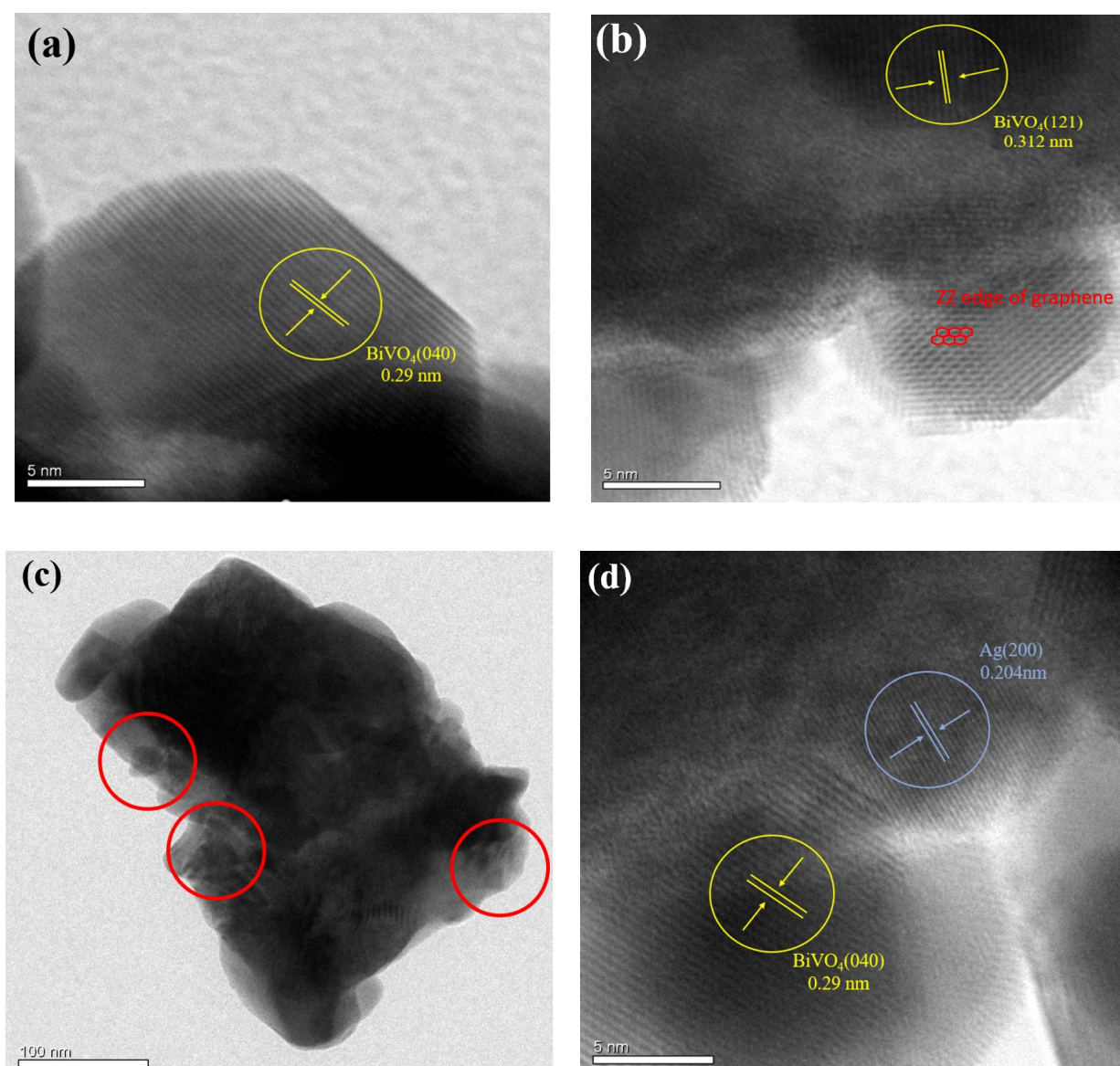


Figure 3. TEM images of the as-prepared photocatalysts. (a) HR-TEM image of pure BiVO_4 ; (b) HR-TEM image of 7 wt% graphene/ BiVO_4 ; (c) low-resolution TEM image; (d) HR-TEM image TAgNPt/graphene/ BiVO_4 with 0.003 wt% TAgNPts and 7 wt% graphene.

The optical absorption properties of the as-prepared photocatalysts were investigated using UV-Vis spectroscopy. Compared with bare BiVO_4 , the addition of graphene and AgNPs enhanced light absorption in the visible region of the spectrum. Figure 5a,b show the increase in visible region absorption. This was also detected for TAgNPts/graphene/ BiVO_4 , as shown in Figure 5b. According to Tauc's equation ($ah\nu = K(h\nu - E_g)^{n/2}$ with $n = 1$), the bandgaps of the as-prepared photocatalysts were estimated with similar values, and are shown in Table 2.

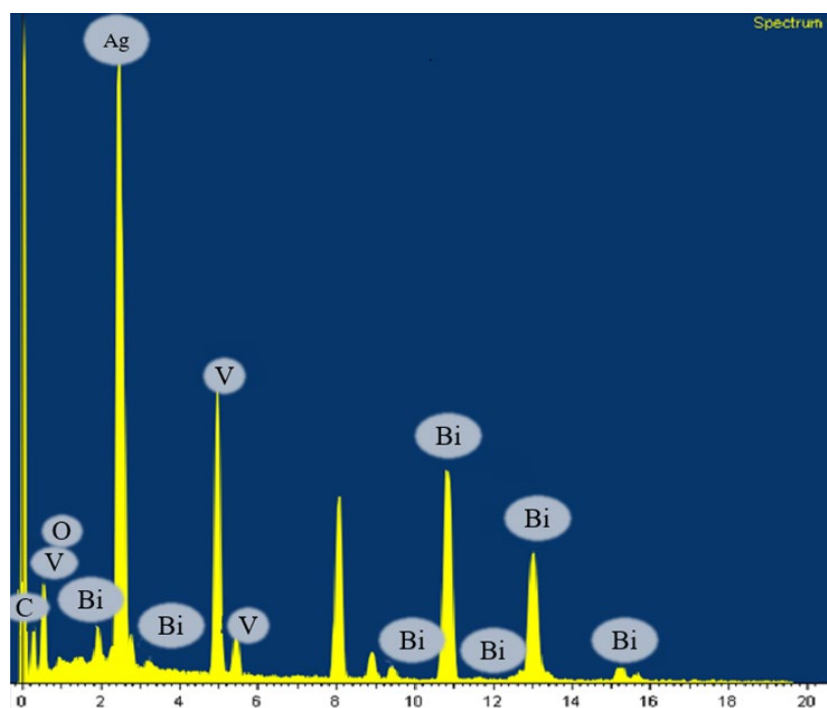


Figure 4. EDS spectrum of 0.003% TAgNPt/7% graphene/BiVO₄.

Table 2. Band gap calculation of the obtained photocatalysts.

Photocatalyst	Band Gap (eV)	Valence Band (eV)	Conduction Band (eV)
BiVO ₄	2.40	1.50	−0.90
7% graphene/BiVO ₄	2.40	–	–
0.1% TAgNPt/7% graphene /BiVO ₄	2.38	1.25	−1.13
0.5 wt% I-AgNP /BiVO ₄	2.40	–	–

– No measurement.

The photoluminescence intensities can indicate the changes in charge recombination rates of different photocatalysts. In Figure 6, it can be observed that the PL spectra of the as-obtained photocatalysts were quite broad, with the phonon band structure corresponding to the transitions from the VB to different phonon levels in the conduction band (CB) of the photocatalysts. Furthermore, the PL intensity of the as-synthesized TAgNPts/graphene/BiVO₄ remarkably decreased compared with that of bulk BiVO₄, suggesting that the recombination rate of photogenerated holes and electrons pairs was suppressed, leading to the improved photocatalytic performance of TAgNPts/graphene/BiVO₄. Figure 7a–e show the XPS spectra of the 0.1% TAgNPt/7% graphene/BiVO₄, which exhibited several peaks that we attributed to the binding energies of Bi 4f, V 2p, C 1s, O 1s, and Ag 3d. Figure 7a shows two peaks with 158 and 164 eV binding energies, which were attributed to Bi 4f_{7/2} and Bi 4f_{5/2}, respectively. The fact that these two peaks are symmetrical in shape, without shoulders, indicates that only one oxidation state of Bi, i.e., Bi³⁺, was present in the as-prepared catalyst. Figure 7b shows two peaks at 516 and 524 eV, which were assigned to the binding energies of V 2p_{3/2} and V 2p_{1/2}, respectively. Although the observation that peak separation (8 eV) and peak area ratio (close to 2:1) of V 2p_{3/2} and V 2p_{1/2} was consistent with the prediction of spin-orbital coupling, it remains challenging to understand why the peak width of V 2p_{1/2} was much broader than that of V 2p_{3/2}. Figure 7c shows a peak at 529 eV, which we assigned to the binding energy of O 1s. Figure 7d shows one peak at 284 eV, which we assigned to C 1s. Figure 7e shows

two peaks at 367 and 374 eV, which we assigned to the binding energies of the $3d_{5/2}$ and $3d_{3/2}$ of Ag, respectively. Because these two peaks were symmetrical in shape without the presence of shoulder peaks, most of the silver elements in the catalyst were metallic silver. Figure 7f shows the XPS valence band spectrum of BiVO_4 and 0.1 wt% TAgNPt/7% graphene/ BiVO_4 . By linearly extrapolating the low binding energy edge intersecting with the XPS background, the valence band energies (E_{VB}) were calculated to be 1.50 and 1.25 eV for BiVO_4 and 0.1 wt% TAgNPt/7% graphene/ BiVO_4 , respectively. The band gaps (E_{BG}) of BiVO_4 and 0.1 wt% TAgNPt/7% graphene/ BiVO_4 were estimated to be 2.40 and 2.38 eV, respectively, from the UV–Vis spectra. Their conduction band energies (E_{CB}) of BiVO_4 and 0.1 wt% TAgNPt/7% graphene/ BiVO_4 were calculated to be -0.90 and -1.13 eV, respectively, using the equation: $E_{\text{CB}} = E_{\text{VB}} - E_{\text{BG}}$. These band structure data of the different photocatalysts in this study are shown in Table 2.

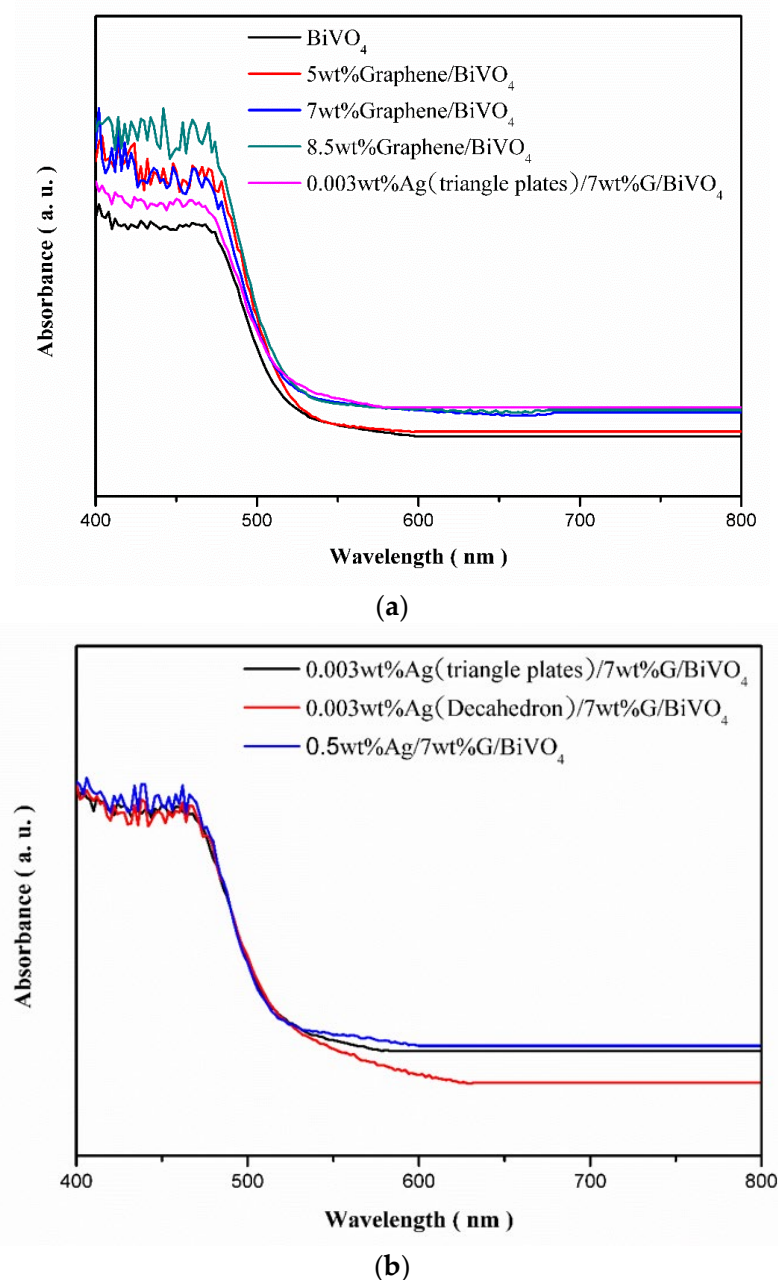


Figure 5. UV–Vis absorption spectra of the obtained photocatalysts (a) by various loading amounts of graphene to BiVO_4 (b) by various kinds of silver on 7% graphene/ BiVO_4 .

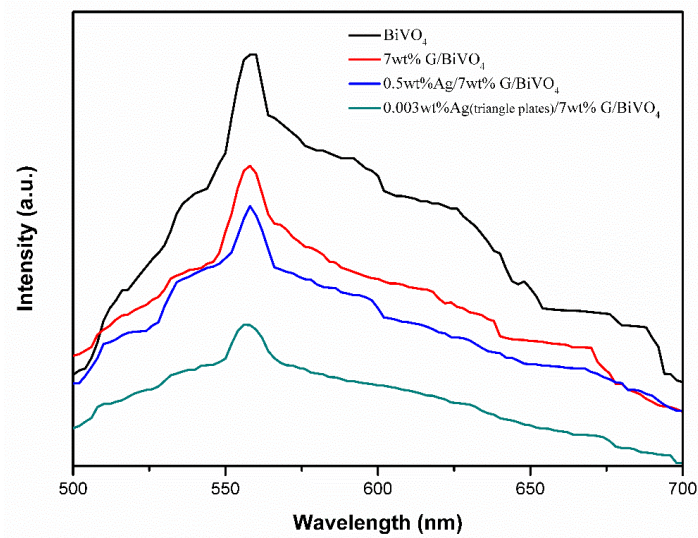


Figure 6. PL spectra of the as-obtained photocatalysts.

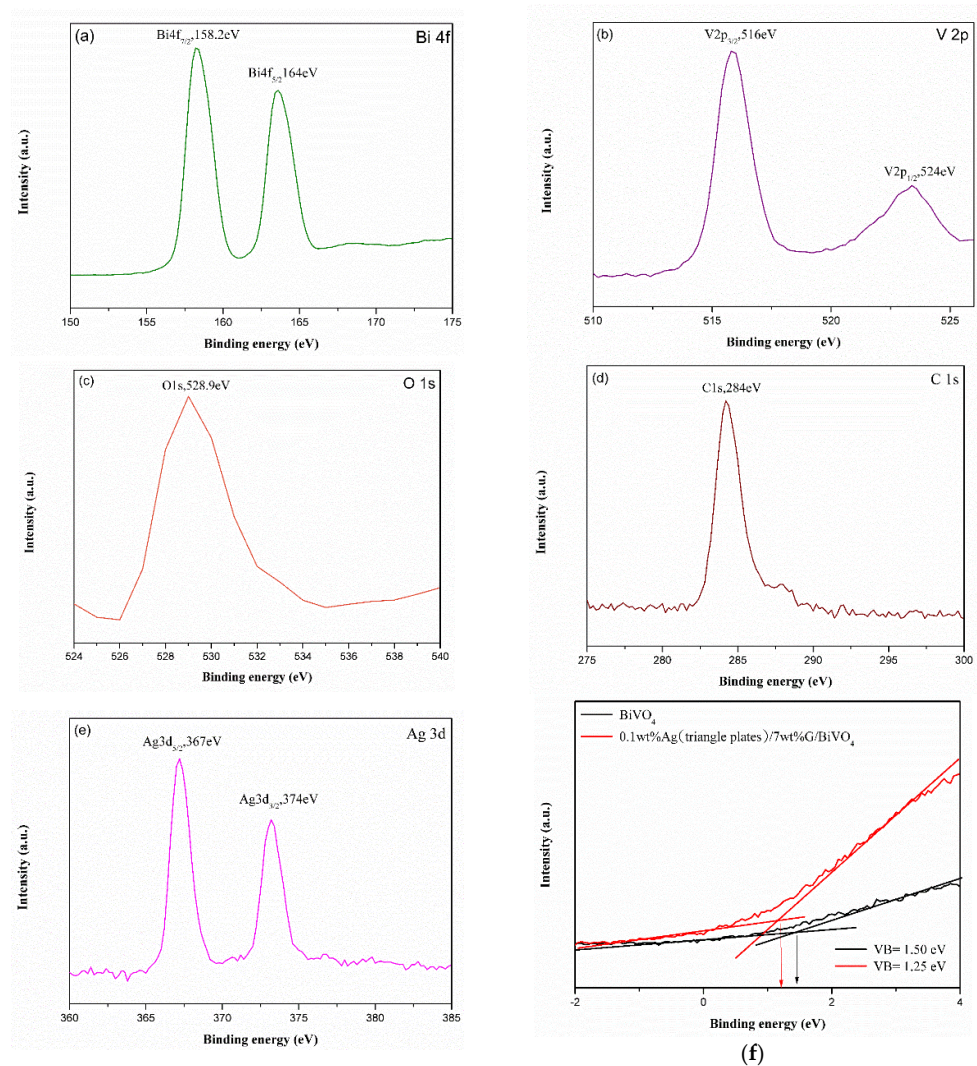


Figure 7. XPS spectra of 0.1% TAGNPt/7% graphene/BiVO₄; (a) Bi 4f spectrum, (b) V 2p spectrum, (c) O 1s spectrum, (d) C 1s spectrum, (e) Ag 3d spectrum, and (f) valence band spectra of BiVO₄ (black) and 0.1 wt% TAGNPt/BiVO₄ (red).

2.2. CO₂ Reduction Activity of Photocatalysts

Figure 8a shows the CH₄ production yields of graphene/BiVO₄ photocatalysts with different amounts of graphene under visible light irradiation. Pure BiVO₄ exhibited the lowest photocatalytic activity, with a CH₄ yield of 28.8 μmolg⁻¹ after 8 h of irradiation. The CH₄ production rate of BiVO₄ was calculated as 3.6 μmolg⁻¹h⁻¹ (Table 3). Through the addition of graphene to BiVO₄, the CH₄ yield and production rate increased, which are shown in Figure 8a and Table 3, respectively. This result occurred due to the increase in visible light absorption intensity caused by the addition of graphene (Figure 5). Because the PL intensity of graphene/BiVO₄ is lower than that of BiVO₄ (Figure 6), another reason might be that the electron in the BiVO₄ conduction band could transfer to graphene, thus decreasing the charge recombination rate and increasing the CH₄ production rate. The CH₄ production rates of graphene/BiVO₄ with different loading amounts of graphene are shown in Table 3. Graphene/BiVO₄ with an optimized loading amount of 7 wt% graphene reached a maximum CH₄ production rate of 7.7 μmolg⁻¹h⁻¹.

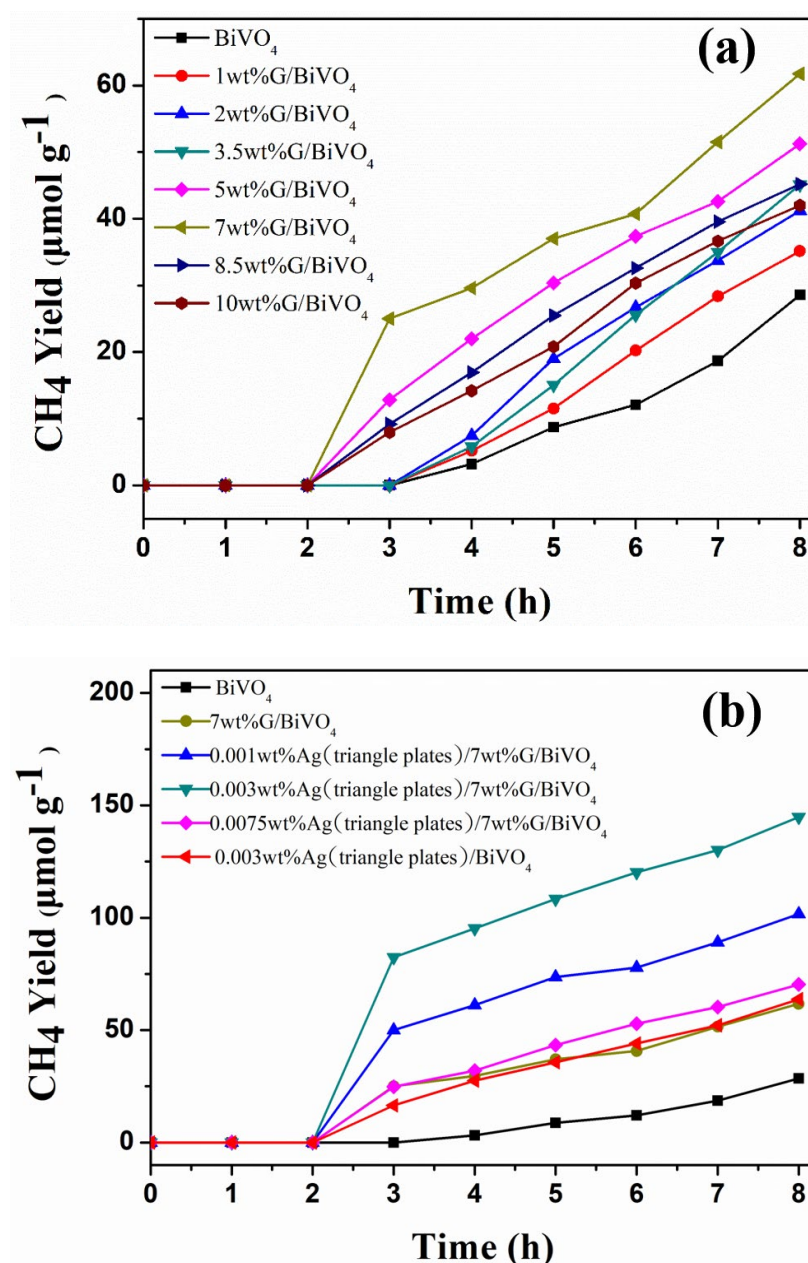


Figure 8. Production yields of CH₄ over the as-obtained photocatalysts.

Table 3. Production rate of CH₄ on various loading of graphene with BiVO₄.

Photocatalysts	Rate of CH ₄ (μmol g ⁻¹ h ⁻¹)
TiO ₂ (P25)	0.4
BiVO ₄	3.6
1 wt% graphene/BiVO ₄	4.4
2 wt% graphene/BiVO ₄	5.2
3.5 wt% graphene/BiVO ₄	5.6
5 wt% graphene/BiVO ₄	6.4
7 wt% graphene/BiVO ₄	7.7
8.5 wt% graphene/BiVO ₄	5.7
10 wt% graphene/BiVO ₄	5.3

Figure 8b reveals that the CH₄ production yield could be further promoted by adding TAgNPs to 7% graphene/BiVO₄. For the TAgNPs' unique optical properties, the enhancing absorption of visible light was studied, as shown in Figure 5. Interestingly, the CH₄ yield first increased with the introduction of AgNPs, and then decreased with increasing loading amounts of AgNPs. After 8 h of irradiation, the production yield of CH₄ reached 144.8 μmolg⁻¹. The optimal loading amount of AgNPs was 0.003 wt%, which is shown in Table 4 and Figure 8b.

Table 4. Production rate of CH₄ on various photocatalysts.

Photocatalysts	Rate of CH ₄ (μmol g ⁻¹ h ⁻¹)
BiVO ₄	3.6
7 wt% graphene/BiVO ₄	7.7
0.001 wt% TAgNPs/7 wt% graphene/BiVO ₄	12.7
0.003 wt% TAgNPs/7 wt% graphene/BiVO ₄	18.1
0.0075 wt% TAgNPs/7 wt% graphene/BiVO ₄	8.8
0.003 wt% D-AgNPs/7 wt% graphene/BiVO ₄	8.4
0.003 wt% I-AgNPs/7 wt% graphene/BiVO ₄	7.0
0.5 wt% I-AgNPs/7 wt% graphene/BiVO ₄	4.5

Table 4 shows the CH₄ production rates of various photocatalysts. Loading 7 wt% graphene/BiVO₄ with decahedral silver nanoparticles (D-AgNPs) and triangular silver nanoplates (TAgNPs) improved the CH₄ production rates. In contrast, loading icosahedral silver nanoparticles (I-AgNPs) depressed the production rate. This is because AgNPs can not only act as electron acceptors to block the electron–hole recombination on BiVO₄, but can also exhibit plasmonic effects. AgNPs with quite different LSPR bands (or shapes) can be synthesized by choosing light with different wavelengths, even in the absence of surfactants. In order to compare the plasmonic effect of AgNPs with different shapes, I-AgNPs (λ_{LSPR} = 410 nm), D-AgNPs (λ_{LSPR} = 490 nm), and TAgNPs (λ_{LSPR} = 680 nm) were prepared using the photochemical method. Figure 9 shows the extinction spectra and the morphologies of these three kinds of AgNP colloids. The extinction spectra show that the LSPR bands of TAgNPs were broader or more intense in the visible range than those of D-AgNPs and I-AgNPs. In particular, TAgNPs generated stronger local fields under visible light irradiation than D-AgNPs and I-AgNPs. Additionally, TAgNPs with sharper corners could help generate stronger local fields than D-AgNPs and I-AgNPs [33]. After performing a series of experiments, an optimal loading amount (0.003 wt%) of TAgNPs was found on 7 wt% graphene/BiVO₄ to achieve the maximum CH₄ production rate. Through calculations, the corresponding quantum efficiency [15] of 0.003 wt% TAgNPs/7 wt% graphene/BiVO₄ was determined to be 0.49%.

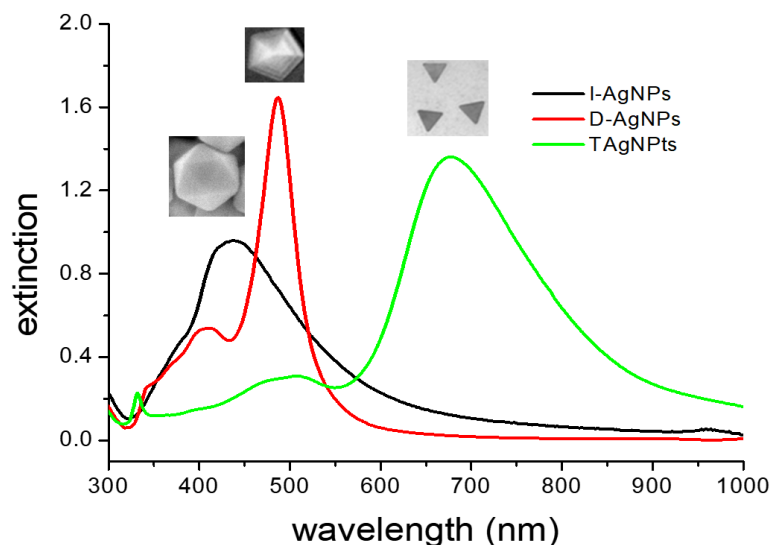


Figure 9. The extinction spectra and the morphologies of I-AgNP, D-AgNP, and TAgNPt colloids.

Stability is one of the primary parameters used for evaluating the performance of photocatalysts. Recycling experiments were conducted, and the results are displayed in Figure 10. After each run, the photocatalysts were recovered by drying in an oven at 373 K and reused for the next run. We observed that 0.003% TAgNPts/7% graphene/BiVO₄ exhibited only a slight decrease in CH₄ yield after three consecutive runs (maintained at approximately 97% from the first cycle), indicating that the as-prepared TAgNPts/graphene/BiVO₄ demonstrated outstanding stability for CO₂ photoreduction.

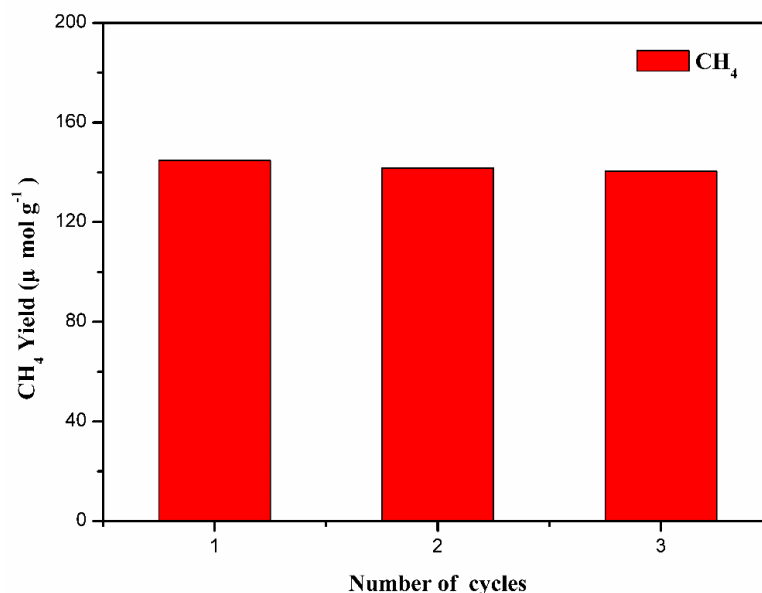


Figure 10. Recycling stability tests over the as-obtained 0.003%TAgNPt/7% graphene/BiVO₄.

2.3. Mechanism of the CO₂ Reduction Reaction

According to the above results and the corresponding analysis, a possible mechanism for the as-prepared TAgNPts/graphene/BiVO₄ on the photocatalytic CO₂ reduction process is proposed by Equations (1) to (6) and described in Figure 11. The electrons in the valence band (VB) were excited through light absorption to the conduction band (CB) of BiVO₄ and generated electron–hole pairs (Equation (1)). Subsequently, a portion of electrons on the CB of BiVO₄ can transfer to graphene and TAgNPts (Equations (3) and (4)) [30,34].

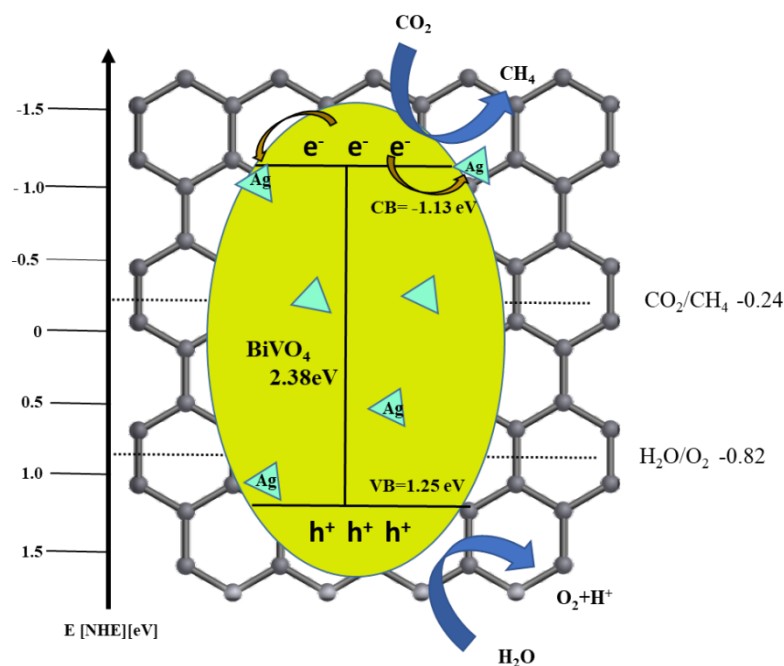
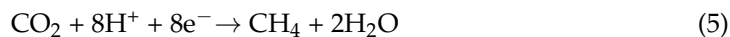
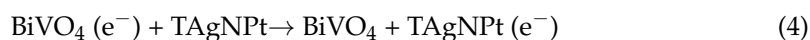
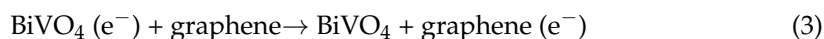
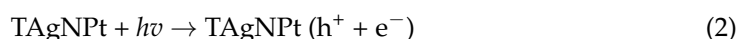
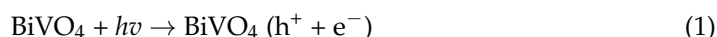


Figure 11. Proposed mechanism for CO₂ photoreduction over the as-obtained TAgNPt/Graphene/BiVO₄.

These energetic electrons can reduce CO₂ to form CH₄ (Equation (5)). There are many possible pathways in this CO₂ photoconversion process, which are not discussed in this paper, but have been described in more detail in previous studies [8,35–37]. Here, graphene and TAgNPs can act as excellent electron acceptors [38,39], successfully preventing the recombination of the charge pairs on BiVO₄. These remaining holes can oxidate H₂O to form O₂ and H⁺ (Equation (6)) [35–37].

Hot electrons and hot holes can also be generated from the decay of excited LSPR of TAgNPs (Equation (2)) [40,41]. In addition, the strong localized electric fields, produced by LSPRs of TAgNPs, may possibly play an important role in enhancing the probability of charge transfer [42].



3. Experiment

3.1. Materials

Bismuth(III)nitrate pentahydrate (Bi(NO₃)₃•5H₂O) from Alfa chemical company with 97% purity; ammonium metavanadate (NH₄VO₃), ethanol (C₂H₅OH), and ethylenediaminetetraacetic acid (EDTA) were obtained from Sigma Aldrich (>99%). Silver nitrate, sodium citrate, and sodium borohydride were purchased from Sigma-Aldrich (St. Louis, MO, USA). Graphene samples were provided by Chiou Shang Co., Ltd. Sodium hydroxide (NaOH, AR grade) was purchased from J. T. Baker (Phillipsburg, NJ, USA). All chemicals were used without any further purification. Milli-Q grade water (>18 M) was used in all of the experiments.

3.2. Preparation of Graphene/BiVO₄ Catalyst and Ag Nanomaterials

As is typical, 5 mmol of Bi(NO₃)₃·5H₂O and a certain amount of graphene were dissolved in 20 mL of HNO₃ (2 M) with the aid of ultrasound for 1 h to form solution A, while 5 mmol of NH₄VO₃ and 3.4 mmol of EDTA were dissolved in 15 mL of NaOH (2 M) to form solution B. Then, the above two solutions were mixed, and the pH value of the solution was adjusted to 6.0 using a NaOH solution (2 M) under magnetic stirring for 0.5 h. Subsequently, the solution was poured into a Teflon-lined hydrothermal autoclave, and then baked in the oven at 180 °C for 6 h, followed by filtering and washing with deionized (DI) water and ethanol several times. Then, the solution was mixed with different amounts of graphene and dried at 80 °C for 12 h to harvest a series of graphene/BiVO₄.

For the purpose of comparing the plasmonic effect of the AgNPs with different morphologies, three kinds of AgNPs, including decahedral silver nanoparticles (D-AgNPs), icosahedral silver nanoparticles (I-AgNPs), and triangular silver nanoplates (TAgNPs), were synthesized using the plasmon-mediated process or photochemical methods according to previous studies [43–45]. A solution was prepared using a mixture of 1 mL of 1.0×10^{-2} M silver nitrate (AgNO₃), 1 mL of 3.0×10^{-2} M sodium citrate, and 97.0 mL DI water. Subsequently, 1 mL of 5.0×10^{-3} M sodium borohydride (NaBH₄) was added dropwise to the ice-cold mixture under magnetic stirring. The colorless solution immediately turned bright yellow after the addition of NaBH₄. The bright yellow color indicated the formation of silver nanoseeds. Subsequently, the silver seed solution was irradiated for 90 min with a 400 W sodium lamp (Philips, average intensity per area ≈ 120 mW/cm²). The solution changed color from yellow to blue, indicating the formation of triangular silver nanoplates (T-AgNPs). D-AgNPs and I-AgNPs were obtained using a seed-free photo-assisted citrate reduction method under the irradiation of blue and violet LEDs, respectively [46]. As in a typical synthesis, 0.5 mL of sodium citrate (4.5×10^{-1} M) and 0.5 mL of AgNO₃ (1.0×10^{-2} M) were mixed with 49.0 mL of pure water. Subsequently, the mixture was irradiated with blue LEDs ($\lambda_{\max} = 476$ nm, average intensity per area ≈ 80 mW/cm²) or violet LEDs ($\lambda_{\max} = 405$ nm, average intensity per area ≈ 60 mW/cm²). The colloidal solutions colored orange and yellow corresponded to the formations of D-AgNPs and I-AgNPs, respectively, after 90 min of LED irradiation.

3.3. Fabrication of Ag/Graphene/BiVO₄ Composites

The as-obtained graphene/BiVO₄ was added to the aqueous solution with different amounts of nano-Ag colloids (I-AgNPs, D-AgNPs, and TAgNPs) under continuous stirring for 0.5 h in the dark, before further irradiation under UV light for 2 h. The colloidal suspension was then centrifuged at 5000 g for 30 min, and the sediment was washed with DI water and dried at 80 °C for 12 h to obtain a series of AgNP/graphene/BiVO₄.

3.4. XRD, SEM, TEM/EDS, UV-Vis, PL and XPS

The structural properties of as-prepared photocatalysts were characterized by the powder X-ray diffraction (XRD) method. The XRD spectra of all samples were measured using a powder XRD diffractometer (XRD-6000, Shimadzu Corp.) with Cu K α radiation ($\lambda = 1.5404$ Å) at a scanning rate of 2°/min in the 2 θ range of 10° to 80°. The average crystalline size (grain size) of the as-obtained photocatalysts was estimated using the Debye–Scherrer formula, $D = \kappa\lambda/\beta\cos\theta$, where κ is 0.9, λ is the wavelength of the X-ray, θ is the Bragg angle, and β is the full width at half the maximum intensity (FWHM) of the diffraction peak. TEM images were obtained using a JEOL-JEM2100F operated at 200 kV. Samples for TEM measurements were dispersed in ethanol, and then a drop was placed on carbon-coated copper grids, followed by drying in ambient conditions. Energy dispersive X-ray spectroscopy (EDS) was used for elemental analysis. Extinction spectra were recorded using a T90+ UV-Vis spectrometer (PG Instrument Ltd.). The photoluminescence spectra (PL) were measured using an Edinburgh FS5 fluorescence spectrometer assembled with an ozone-free xenon lamp. The electronic structures of nanocomposites were analyzed

by X-ray photoelectron spectroscopy (XPS) using a PHI 5000 versaprobe/scanning ESCA microprobe photoelectron spectroscopy with Mono Al K α radiation.

3.5. Photocatalytic Reduction of CO₂

Figure 12 shows the experimental setup for the CO₂ photoreduction and analysis system. Generally, 0.05 g of the as-prepared photocatalyst was placed and evenly distributed in a Pyrex glass container. High-purity CO₂, regulated using a mass flow controller (15 mL min⁻¹, 35 min), passed through a water bubbler to obtain a H₂O/CO₂ mixture. The glass container was irradiated under a 400 W high-pressure Hg lamp. The products (gas phase) were collected and analyzed using an online gas chromatograph (Gas Chromatography Personal GC 1000, Taipei, Taiwan) equipped with a Carboxen 1000 packed column at various times during the photoreaction. Each experiment was performed at least three times.

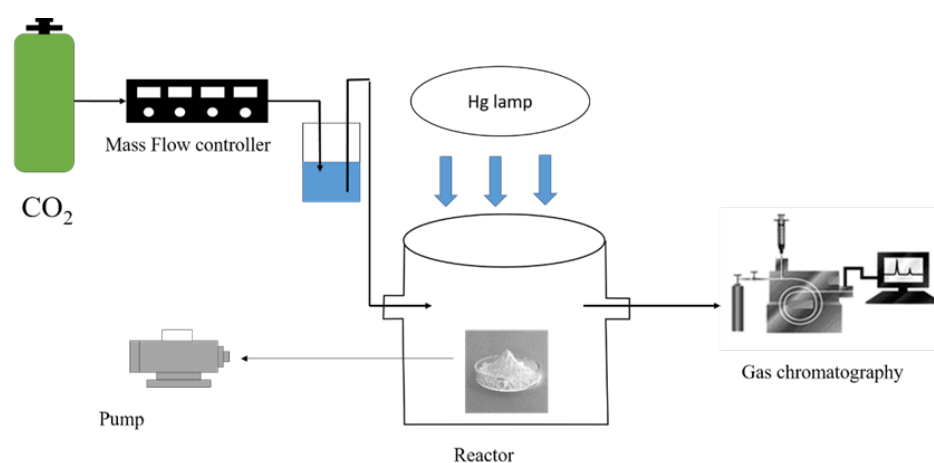


Figure 12. Schematic of the experimental setup for CO₂ photoreduction.

4. Conclusions

In summary, pure BiVO₄, graphene/BiVO₄, and AgNPs/graphene/BiVO₄ photocatalysts with different loading ratios were synthesized to enhance the efficiency of CO₂ conversion to CH₄ under light irradiation. Our experimental results demonstrated that the as-obtained TAgNPs/graphene/BiVO₄ with 7 wt% graphene and 0.003 wt% Ag exhibited optimum photocatalytic activity, about 5.03 times higher than that of pure BiVO₄. Moreover, a possible mechanism for CO₂ photoreduction was proposed based on the experimental data and results of this study. Therefore, this work introduced a feasible strategy to potentially design an effective photocatalyst for CO₂ photoreduction.

Author Contributions: Conceptualization, C.-L.H. and R.-J.W.; methodology, R.-J.W.; software, B.-X.J.; validation, B.-X.J.; formal analysis, B.-X.J.; investigation, B.-X.J.; resources, Y.C.; data curation, B.-X.J.; writing—original draft preparation, Z.Z.; writing—review and editing, C.-L.H. and R.-J.W.; supervision, R.-J.W.; project administration, R.-J.W.; funding acquisition, R.-J.W. All authors have read and agreed to the published version of the manuscript.

Funding: This research was funded by the Ministry of Science and Technology (Grant No.: MOST 110-2113-M-126-001), Taiwan.

Institutional Review Board Statement: Not applicable.

Informed Consent Statement: Not applicable.

Data Availability Statement: Not applicable.

Acknowledgments: The authors would like to thank the Ministry of Science and Technology (grant No.: MOST 110-2113-M-126-001), Taiwan, R.O.C., for the financial support that it provided for this study.

Conflicts of Interest: The authors declare no conflict of interest.

References

1. Leung, D.Y.C.; Caramanna, G.; Maroto-Valer, M.M. An overview of current status of carbon dioxide capture and storage technologies. *Renew. Sustain. Energy Rev.* **2014**, *39*, 426–443. [[CrossRef](#)]
2. Wilberforce, T.; Baroutaji, A.; Soudan, B.; Al-Alami, A.H.; Olabi, A.G. Outlook of carbon capture technology and challenges. *Sci. Total Environ.* **2019**, *657*, 56–72. [[CrossRef](#)] [[PubMed](#)]
3. Artz, J.; Müller, T.E.; Thenert, K.M.; Kleinekorte, J.; Meys, R.; Sternberg, A.; Bardow, A.; Leitner, W. Sustainable Conversion of Carbon Dioxide: An Integrated Review of Catalysis and Life Cycle Assessment. *Chem. Rev.* **2018**, *118*, 434–504. [[CrossRef](#)] [[PubMed](#)]
4. Birdja, Y.Y.; Pérez-Gallent, E.; Figueiredo, M.C.; Göttle, A.J.; Calle-Vallejo, F.; Koper, M.T.M. Advances and challenges in understanding the electrocatalytic conversion of carbon dioxide to fuels. *Nat. Energy* **2019**, *4*, 732–745. [[CrossRef](#)]
5. Li, K.; Peng, B.; Peng, T. Recent Advances in Heterogeneous Photocatalytic CO₂ Conversion to Solar Fuels. *ACS Catal.* **2016**, *6*, 7485–7527. [[CrossRef](#)]
6. Tu, W.; Zhou, Y.; Zou, Z. Photocatalytic conversion of CO₂ into renewable hydrocarbon fuels: State-of-the-art accomplishment, challenges, and prospects. *Adv. Mater.* **2014**, *26*, 4607–4626. [[CrossRef](#)] [[PubMed](#)]
7. Shehzad, N.; Tahir, M.; Johari, K.; Murugesan, T.; Hussain, M. A critical review on TiO₂ based photocatalytic CO₂ reduction system: Strategies to improve efficiency. *J. CO₂ Util.* **2018**, *26*, 98–122. [[CrossRef](#)]
8. Habisreutinger, S.N.; Schmidt-Mende, L.; Stolarczyk, J.K. Photocatalytic reduction of CO₂ on TiO₂ and other semiconductors. *Angew. Chem. Int. Ed.* **2013**, *52*, 7372–7408. [[CrossRef](#)]
9. Han, B.; Song, J.; Liang, S.; Chen, W.; Deng, H.; Ou, X.; Xu, Y.-J.; Lin, Z. Hierarchical NiCo₂O₄ hollow nanocages for photoreduction of diluted CO₂: Adsorption and active sites engineering. *Appl. Catal. B Environ.* **2020**, *260*, 118208. [[CrossRef](#)]
10. Li, H.; Zhang, L.; Cao, Y. Synthesis of palladium-modified MnS photocatalysts with enhanced photocatalytic activity in the photoreduction of CO₂ to CH₄. *Appl. Surf. Sci.* **2021**, *541*, 148519. [[CrossRef](#)]
11. Shi, Q.; Huang, J.; Yang, Y.; Wu, J.; Shen, J.; Liu, X.; Sun, A.; Liu, Z. In-situ construction of urchin-like hierarchical g-C₃N₄/NiAl-LDH hybrid for efficient photoreduction of CO₂. *Mater. Lett.* **2020**, *268*, 127560. [[CrossRef](#)]
12. Xiao, L.; Lin, R.; Wang, J.; Cui, C.; Wang, J.; Li, Z. A novel hollow-hierarchical structured Bi₂WO₆ with enhanced photocatalytic activity for CO₂ photoreduction. *J. Colloid Interface Sci.* **2018**, *523*, 151–158. [[CrossRef](#)]
13. Li, B.; Sun, L.; Bian, J.; Sun, N.; Sun, J.; Chen, L.; Li, Z.; Jing, L. Controlled synthesis of novel Z-scheme iron phthalocyanine/porous WO₃ nanocomposites as efficient photocatalysts for CO₂ reduction. *Appl. Catal. B Environ.* **2020**, *270*, 118849. [[CrossRef](#)]
14. Wang, Y.; Zhang, X.; Zhang, C.; Li, R.; Wang, Y.; Fan, C. Novel Bi₄Ti₃O₁₂ hollow-spheres with highly-efficient CO₂ photoreduction activity. *Inorg. Chem. Commun.* **2020**, *116*, 107931. [[CrossRef](#)]
15. Huang, Y.F.; Liao, K.W.; Fahmi, F.R.Z.; Modak, V.A.; Tsai, S.H.; Ke, S.W.; Wang, C.H.; Chen, L.C.; Chen, K.H. Thickness-Dependent Photocatalysis of Ultra-Thin MoS₂ Film for Visible-Light-Driven CO₂ Reduction. *Catalysts* **2021**, *11*, 1295. [[CrossRef](#)]
16. Zhu, Z.; Yang, C.-X.; Hwang, Y.-T.; Lin, Y.-C.; Wu, R.-J. Fuel generation through photoreduction of CO₂ on novel Cu/BiVO₄. *Mater. Res. Bull.* **2020**, *130*, 110955. [[CrossRef](#)]
17. Zhu, Z.; Hwang, Y.T.; Liang, H.C.; Wu, R.J. Prepared Pd/MgO/BiVO₄ composite for photoreduction of CO₂ to CH₄. *J. Chin. Chem. Soc.* **2021**, *68*, 1897–1907. [[CrossRef](#)]
18. Wei, Z.-H.; Wang, Y.-F.; Li, Y.-Y.; Zhang, L.; Yao, H.-C.; Li, Z.-J. Enhanced photocatalytic CO₂ reduction activity of Z-scheme CdS/BiVO₄ nanocomposite with thinner BiVO₄ nanosheets. *J. CO₂ Util.* **2018**, *28*, 15–25. [[CrossRef](#)]
19. Rather, R.A.; Khan, M.; Lo, I.M. High charge transfer response of g-C₃N₄/Ag/AgCl/BiVO₄ microstructure for the selective photocatalytic reduction of CO₂ to CH₄ under alkali activation. *J. Catal.* **2018**, *366*, 28–36. [[CrossRef](#)]
20. Han, Q.; Li, L.; Gao, W.; Shen, Y.; Wang, L.; Zhang, Y.; Wang, X.; Shen, Q.; Xiong, Y.; Zhou, Y.; et al. Elegant Construction of ZnIn₂S₄/BiVO₄ Hierarchical Heterostructures as Direct Z-Scheme Photocatalysts for Efficient CO₂ Photoreduction. *ACS Appl. Mater. Interfaces* **2021**, *13*, 15092–15100. [[CrossRef](#)]
21. Lincic, S.; Christopher, P.; Ingram, D.B. Plasmonic-metal nanostructures for efficient conversion of solar to chemical energy. *Nat. Mater.* **2011**, *10*, 911–921. [[CrossRef](#)]
22. Hsu, H.-L.; Juang, T.-Y.; Chen, C.-P.; Hsieh, C.-M.; Yang, C.-C.; Huang, C.-L.; Jeng, R.-J. Enhanced efficiency of organic and perovskite photovoltaics from shape-dependent broadband plasmonic effects of silver nanoplates. *Sol. Energy Mater. Sol. Cells* **2015**, *140*, 224–231. [[CrossRef](#)]
23. Zhang, X.; Chen, Y.L.; Liu, R.-S.; Tsai, D.P. Plasmonic photocatalysis. *Rep. Prog. Phys.* **2013**, *76*, 046401. [[CrossRef](#)]
24. Bao, Q.; Loh, K.P. Graphene Photonics, Plasmonics, and Broadband Optoelectronic Devices. *ACS Nano* **2012**, *6*, 3677–3694. [[CrossRef](#)] [[PubMed](#)]

25. Choi, H.; Ko, S.-J.; Choi, Y.; Joo, P.; Kim, T.; Lee, B.R.; Jung, J.-W.; Choi, H.J.; Cha, M.; Jeong, J.-R.; et al. Versatile surface plasmon resonance of carbon-dot-supported silver nanoparticles in polymer optoelectronic devices. *Nat. Photonics* **2013**, *7*, 732–738. [[CrossRef](#)]
26. Jin, R.; Cao, Y.; Mirkin, C.A.; Kelly, K.L.; Schatz, G.C.; Zheng, J.G. Photoinduced Conversion of Silver Nanospheres to Nanoprisms. *Science* **2001**, *294*, 1901–1903. [[CrossRef](#)] [[PubMed](#)]
27. Jin, R.; Cao, Y.C.; Hao, E.; Métraux, G.S.; Schatz, G.C.; Mirkin, C.A. Controlling anisotropic nanoparticle growth through plasmon excitation. *Nature* **2003**, *425*, 487–490. [[CrossRef](#)] [[PubMed](#)]
28. Zhang, Q.; Ge, J.; Pham, T.; Goebel, J.; Hu, Y.; Lu, Z.; Yin, Y. Reconstruction of Silver Nanoplates by UV Irradiation: Tailored Optical Properties and Enhanced Stability. *Angew. Chem. Int. Ed.* **2009**, *48*, 3516–3519. [[CrossRef](#)]
29. Lee, B.-H.; Hsu, M.-S.; Hsu, Y.-C.; Lo, C.-W.; Huang, C.-L. A Facile Method to Obtain Highly Stable Silver Nanoplate Colloids with Desired Surface Plasmon Resonance Wavelengths. *J. Phys. Chem. C* **2010**, *114*, 6222–6227. [[CrossRef](#)]
30. Zhu, Z.; Lin, Y.-C.; Chung, C.-L.; Wu, R.-J.; Huang, C.-L. A novel composite of triangular silver nanoplates on BiVO₄ for gaseous formaldehyde degradation. *Appl. Surf. Sci.* **2021**, *543*, 148784. [[CrossRef](#)]
31. Lin, W.-D.; Liao, C.-T.; Chang, T.-C.; Chen, S.-H.; Wu, R.-J. Humidity sensing properties of novel graphene/TiO₂ composites by sol-gel process. *Sens. Actuators B Chem.* **2015**, *209*, 555–561. [[CrossRef](#)]
32. Zhang, A.; Zhang, J. Synthesis and characterization of Ag/BiVO₄ composite photocatalyst. *Appl. Surf. Sci.* **2010**, *256*, 3224–3227. [[CrossRef](#)]
33. Guo, R.; Yan, A.; Xu, J.; Xu, B.; Li, T.; Liu, X.; Yi, T.; Luo, S. Effects of morphology on the visible-light-driven photocatalytic and bactericidal properties of BiVO₄/CdS heterojunctions: A discussion on photocatalysis mechanism. *J. Alloys Compd.* **2020**, *817*, 153246. [[CrossRef](#)]
34. Okoth, O.K.; Yan, K.; Zhang, J. Mo-doped BiVO₄ and graphene nanocomposites with enhanced photoelectrochemical performance for aptasensing of streptomycin. *Carbon* **2017**, *120*, 194–202. [[CrossRef](#)]
35. Lingampalli, S.R.; Ayyub, M.M.; Rao, C.N.R. Recent Progress in the Photocatalytic Reduction of Carbon Dioxide. *ACS Omega* **2017**, *2*, 2740–2748. [[CrossRef](#)]
36. Ma, Y.; Wang, X.; Jia, Y.; Chen, X.; Han, H.; Li, C. Titanium Dioxide-Based Nanomaterials for Photocatalytic Fuel Generations. *Chem. Rev.* **2014**, *114*, 9987–10043. [[CrossRef](#)]
37. Kubacka, A.; Fernández-García, M.; Colón, G. Advanced Nanoarchitectures for Solar Photocatalytic Applications. *Chem. Rev.* **2012**, *112*, 1555–1614. [[CrossRef](#)]
38. Xiang, Q.; Yu, J.; Jaroniec, M. Graphene-based semiconductor photocatalysts. *Chem. Soc. Rev.* **2012**, *41*, 782–796. [[CrossRef](#)]
39. Zhu, X.; Liang, X.; Wang, P.; Dai, Y.; Huang, B. Porous Ag-ZnO microspheres as efficient photocatalyst for methane and ethylene oxidation: Insight into the role of Ag particles. *Appl. Surf. Sci.* **2018**, *456*, 493–500. [[CrossRef](#)]
40. Brongersma, M.L.; Halas, N.J.; Nordlander, P. Plasmon-induced hot carrier science and technology. *Nat. Nanotechnol.* **2015**, *10*, 25–34. [[CrossRef](#)]
41. Clavero, C. Plasmon-induced hot-electron generation at nanoparticle/metal-oxide interfaces for photovoltaic and photocatalytic devices. *Nat. Photonics* **2014**, *8*, 95–103. [[CrossRef](#)]
42. Christopher, P.; Moskovits, M. Hot Charge Carrier Transmission from Plasmonic Nanostructures. *Annu. Rev. Phys. Chem.* **2017**, *68*, 379–398. [[CrossRef](#)] [[PubMed](#)]
43. Yang, L.-C.; Lai, Y.-S.; Tsai, C.-M.; Kong, Y.-T.; Lee, C.-I.; Huang, C.-L. One-Pot Synthesis of Monodispersed Silver Nanodecahedra with Optimal SERS Activities Using Seedless Photo-Assisted Citrate Reduction Method. *J. Phys. Chem. C* **2012**, *116*, 24292–24300. [[CrossRef](#)]
44. Xie, Z.-X.; Tzeng, W.-C.; Huang, C.-L. One-Pot Synthesis of Icosahedral Silver Nanoparticles by Using a Photoassisted Tartrate Reduction Method under UV Light with a Wavelength of 310 nm. *ChemPhysChem* **2016**, *17*, 2551–2557. [[CrossRef](#)]
45. Ciou, S.-H.; Cao, Y.-W.; Huang, H.-C.; Su, D.-Y.; Huang, C.-L. SERS Enhancement Factors Studies of Silver Nanoprism and Spherical Nanoparticle Colloids in The Presence of Bromide Ions. *J. Phys. Chem. C* **2009**, *113*, 9520–9525. [[CrossRef](#)]
46. Kelly, K.L.; Coronado, E.; Zhao, L.L.; Schatz, G.C. The Optical Properties of Metal Nanoparticles: The Influence of Size, Shape, and Dielectric Environment. *J. Phys. Chem. B* **2003**, *107*, 668–677. [[CrossRef](#)]